Boron phosphide as a *p*-type transparent conductor: Optical absorption and transport through electron-phonon coupling

Viet-Anh Ha [1,*] Bora Karasulu [2] Ryo Maezono,[3] Guillaume Brunin [1] Joel Basile Varley,[4] Gian-Marco Rignanese [1] Bartomeu Monserrat,[2,5,†] and Geoffroy Hautier[1,‡]

[1]*Institute of Condensed Matter and Nanoscience (IMCN), Université catholique de Louvain (UCL),*
Chemin étoiles 8, bte L7.03.01, Louvain-la-Neuve 1348, Belgium
[2]*Cavendish Laboratory, University of Cambridge, J. J. Thomson Avenue, Cambridge CB3 0HE, United Kingdom*
[3]*School of Information Science, JAIST, Asahidai 1-1, Nomi, Ishikawa 923-1292, Japan*
[4]*Lawrence Livermore National Laboratory 7000 East Avenue, L-413 Livermore, California 94550, USA*
[5]*Department of Materials Science and Metallurgy, University of Cambridge, 27 Charles Babbage Road,*
Cambridge CB3 0FS, United Kingdom

Boron phosphide has recently been identified as a potential high-hole-mobility transparent conducting material. This promise arises from its low hole effective masses. However, boron phosphide has a relatively small, 2 eV, indirect bandgap which will affect its transparency. In this work, we computationally study both optical absorption across the indirect gap and phonon-limited electronic transport to quantify the potential of boron phosphide as a *p*-type transparent conductor. We find that phonon-mediated indirect optical absorption is weak in the visible spectrum and that the phonon-limited hole mobility is very high (around 900 cm^2/Vs) at room temperature. This exceptional mobility comes from the combination of a low hole effective mass and very weak scattering by polar phonon modes. We rationalize the weak scattering by the less ionic bonding in boron phosphide compared to oxides. We suggest that this could be a general advantage of nonoxides for *p*-type transparent conducting applications. Using our computed properties, we assess the transparent conductor figure of merit of boron phosphide and show that it exceeds by one order of magnitude that of established *p*-type transparent conductors, confirming the potential of this material.

I. INTRODUCTION

Transparent conducting materials (TCMs) are necessary to many applications ranging from solar cells to transparent electronics. So far, *n*-type oxides (e.g., In_2O_3, SnO_2, and ZnO) are the highest-performing TCMs, allowing them to be used in commercial devices [1–5]. On the other hand, *p*-type TCMs show poorer performance, especially in terms of carrier mobility, limiting the development of new technologies such as transparent solar cells or transistors [3,6]. Hence, the search for high-performance *p*-type TCMs has been a long-lasting goal of the materials research community.

As demonstrated by analyzing high-throughput computational data, *p*-type oxides have inherently higher effective masses than *n*-type oxides, thus rationalizing the current gap in mobility between the best *p*-type and *n*-type oxides [7,8]. The strong oxygen *p*-orbital character in the valence band of most oxides is responsible for their statistically high hole effective mass. This inherent difficulty in developing *p*-type

transparent oxides with a low hole effective mass justifies moving towards nonoxide TCM chemistries, including fluorides [9], sulfides [10,11], oxyanions [12,13], suboxides [14], or germanides [15]. The opportunities in nonoxide chemistries have been recently confirmed by further analysis of high-throughput computational data showing that nonoxide materials have statistically lower hole effective masses than oxides [16,17]. Unfortunately, these lower hole effective masses come with smaller bandgaps that are detrimental to transparency. Using the difference between fundamental (indirect) and optical (direct) bandgaps, through high-throughput computing we identified boron phosphide (BP) as a very promising *p*-type TCM candidate [16]. Boron phosphide shows, according to computations, a rare combination of a low hole effective mass, a large direct bandgap, and *p*-type dopability.

Boron phosphide was characterized experimentally through electrical and optical measurements [18–26] but the sample quality is variable between these studies and an in-depth theoretical analysis of BP is thus required. In this paper, we theoretically study indirect optical absorption and transport properties of hole carriers in BP. Using state-of-the-art electron-phonon computations, we investigate how phonon-assisted indirect optical transitions impact the transparency of this material. We also use the electron-phonon scattering matrix elements to study transport properties and, especially, hole mobility. We combine these theoretical

---

*Present address: Oden Institute for Computational Engineering and Sciences, University of Texas at Austin, 201 East 24th Street, Austin, Texas 78712, USA.

†bm418@cam.ac.uk

‡geoffroy.hautier@uclouvain.be

II. COMPUTATIONAL DETAILS

A. Indirect optical absorption

The complex dielectric function $\varepsilon_1(E) + i\varepsilon_2(E)$ determines the extinction coefficient $\kappa = [(-\varepsilon_1 + \sqrt{\varepsilon_1^2 + \varepsilon_2^2})/2]^{1/2}$ and the absorption coefficient $\alpha(E) = 2E\kappa(E)/\hbar c$ [27], where E is the photon energy, $\hbar$ is the reduced Planck constant, and c is the speed of light. In the independent-particle approximation and the electric dipole approximation, the frequency-dependent imaginary part of the dielectric function is given by

$$\varepsilon_2(E) = \frac{2\pi}{mN} \frac{\hbar^2 \omega_p^2}{E^2} \sum_{v,c} \int_{\mathrm{BZ}} \frac{d\mathbf{k}}{(2\pi)^3} |M_{cv\mathbf{k}}|^2 \delta(\epsilon_{c\mathbf{k}} - \epsilon_{v\mathbf{k}} - E),$$

$$(1)$$

where m is the electron mass, N is the number of electrons per unit of volume, $\omega_p^2 = Ne^2/\epsilon_0 m$ is the plasma frequency of the solid [28], with e the elementary charge and ϵ_0 the vacuum permittivity, $M_{cv\mathbf{k}} = \langle \psi_{c\mathbf{k}} | \hat{\mathbf{e}} \cdot \mathbf{p} | \psi_{v\mathbf{k}} \rangle$ is the optical matrix element, where $\hat{\mathbf{e}}$ is the polarization of the incident light and $\mathbf{p}$ is the momentum operator, and electronic wave functions $|\psi\rangle$ of energy ϵ and momentum $\mathbf{k}$ are labeled by their valence v or conduction c band index. The factor 2 in Eq. (1) represents the spin degeneracy. The Kramers-Kronig relation [29] gives the real part of the dielectric function $\varepsilon_1(E)$.

The effects of lattice dynamics on the dielectric function at temperature T are introduced by means of the Williams-Lax theory [30,31] as

$$\varepsilon_2(E;T) = \frac{1}{\mathcal{Z}} \sum_{\mathbf{s}} \langle \Phi_{\mathbf{s}}(\mathbf{u}) | \varepsilon_2(E; \mathbf{u}) | \Phi_{\mathbf{s}}(\mathbf{u}) \rangle e^{-E_{\mathbf{s}}/k_B T}, \quad (2)$$

where $|\Phi_{\mathbf{s}}(\mathbf{u})\rangle$ is the harmonic vibrational wave function in state $\mathbf{s}$ with energy $E_{\mathbf{s}}$, $\mathbf{u} = \{u_{\nu\mathbf{q}}\}$ is a collective ionic coordinate in terms of normal modes of vibration $(\nu, \mathbf{q})$, $\mathcal{Z} = \sum_{\mathbf{s}} e^{-E_{\mathbf{s}}/k_B T}$ is the partition function, and k_B is Boltzmann's constant. This expression has recently become amenable to first-principles methods [32–38] and we evaluate it using thermal lines [39,40].

We perform the optical absorption calculations at a finite temperature using density functional theory (DFT) in the projector augmented-wave formulation as implemented in the VASP [41–44]. We perform self-consistent and lattice dynamics calculations using an energy cutoff of 500 eV and an electronic Brillouin zone (BZ) Monkhorst-Pack [45] sampling grid of size $8 \times 8 \times 8$ for the primitive cell and commensurate grids for the supercells. We perform calculations using both the generalized gradient approximation of Perdew-Burke-Ernzerhof (PBE) [46] and the hybrid Heyd-Scuseria-Ernzerhof (HSE) [47] functionals. We calculate the harmonic lattice dynamics using the finite-displacement method in conjunction with nondiagonal supercells [48] using coarse vibrational BZ grids of sizes up to $4 \times 4 \times 4$.

B. Transport properties

From Drude's theory [49], the mobility, written as $\mu = e\tau/m^*$, is proportional to the average relaxation time τ and inversely proportional to the effective mass m^* of carriers. The relaxation time τ (inverse of scattering rate) depends on different scattering mechanisms such as scattering by phonons, ionized and neutral impurities, and grain boundaries. Here, we take into account only the scattering of carriers by phonons, which is likely to be an important component of scattering and is an intrinsic mechanism. The carrier scattering by phonons can be computed theoretically if the electron-phonon coupling matrix elements are known. In principle, one can employ density-functional perturbation theory (DFPT) to obtain the electron-phonon matrix elements from first principles [50–52]. However, convergence of relevant physical properties (e.g., electron scattering rate by phonons) often requires very dense $\mathbf{k}$- and $\mathbf{q}$-point meshes for electrons and phonons, respectively, and a considerable computational time if fully performed within DFPT. The recently developed interpolation techniques based on Wannier functions offer a very practical and efficient solution to overcome this obstacle. Here, we use the EPW code [53,54] interfaced with QUANTUM ESPRESSO (QE) [55,56] to calculate the relaxation time $\tau_{n\mathbf{k}}$ (n is the band index). More details on the theory and the implementation are presented in Ref. [54]. In this work, the electron-phonon interaction matrix elements were computed with QE using DFPT on a coarse $6 \times 6 \times 6$ $\mathbf{q}$-point mesh as a starting point for the interpolation with EPW. $\tau_{n\mathbf{k}}$ is calculated using EPW on dense $80 \times 80 \times 80$ meshes for both the $\mathbf{k}$ point (for electrons) and the $\mathbf{q}$ point (for phonons) to guarantee the convergence. The Fermi level is set correspondingly to each doping concentration. All phonon modes for both interband and intraband scattering mechanisms are taken into account in the computation of scattering rates. The structure relaxation and self-consistent, non-self-consistent, and phonon calculations are performed using the PBE functional and norm-conserving pseudopotentials [57] with very stringent parameters for convergence, e.g., a high cutoff energy of 1088.5 eV (80 Ry).

In order to estimate the hole mobility due to the phonon scattering, we solve Boltzmann's transport equation (BTE) using the BoltzTrap package [58]. The relaxation time $\tau_{n\mathbf{k}}$ obtained with EPW and DFT band structure $\epsilon_{n\mathbf{k}}$ are necessary inputs for BoltzTrap. More details about the calculations can be found in Ref. [17].

C. Figure of merit

In many applications, the quantities of interest for TCMs are the conductivity and transparency. It is convenient to use figure of merit which estimates the performance of a TCM material through one quantity. Different FOMs exist in the literature to compare TCMs [3]. We use the one defined by Haacke [59] as $\overline{T}^{10}\sigma_s$, where $\overline{T}$ is the transparency or transmittance and $\sigma_s = \sigma t$ is the sheet conductivity of a film with thickness t and conductivity σ. The conductivity is simply given by $\sigma = \mu C e$, with μ and C being the hole mobility and concentration, respectively. The average transmittance in the
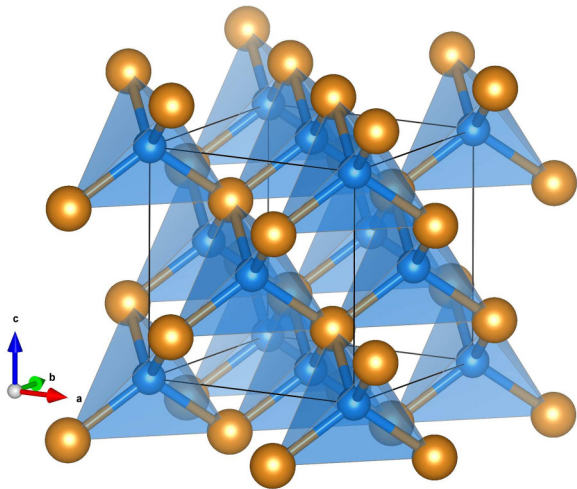
FIG. 1. The conventional BP cell with tetrahedral local environments around B atoms (blue).

visible spectrum is computed as

$$\overline{T} = \frac{\int_{\text{vis}} B_E [1 - R(E)] \exp[-\alpha(E)t] dE}{\int_{\text{vis}} B_E dE}, \qquad (3)$$

where B_E is the spectral radiance of a black body at a temperature of 5778 K to model the solar spectrum, $R(E)$ is the reflectivity, and t is the thickness of a given film. $\alpha(E)$ is computed as the sum of the indirect absorption (the direct absorption is negligible in the visible spectrum as the direct gap of BP > 3 eV [16]) and the absorption due to plasmon effects, which is modeled through the Drude model as in Ref. [60]. The reflectivity is derived from the absorption coefficient and the refractive index, obtained through Kramers-Kronig relations [29]. We compare the FOM of BP with that of a current *p*-type TCM, CuAlO$_2$. For BP, the theoretical mobility and absorption coefficient are used. For CuAlO$_2$, we use a hole mobility of 1 cm^2/Vs [61–64] and an effective mass of 2.5 times the free electron mass [7] as inputs for the Drude model to obtain the transmittance and the conductivity, as in Ref. [60]. In this case, our calculation does not rely on the absorption coefficient but rather on a relative dielectric constant of 11.7 in order to model the 70% transmittance measured in thin films [62]. We neglect the influence of the second gap, which has been theoretically computed for CuAlO$_2$ [65]. For both materials, we consider films of varying thicknesses and hole concentrations.

III. RESULTS AND DISCUSSION

The conventional BP cell is shown in Fig. 1. Each B atom is surrounded by four P atoms in tetrahedral corner-sharing local environments. The cubic symmetry leads to an isotropic effective mass tensor [16]. Figure 2 shows the phonon dispersions (fat bands) and projected density of states (DOS) of phonons for BP using the PBE functional. The fat band representation indicates which atom participates in the phonon modes. The lighter B atoms mainly contribute to the optical modes at high frequencies (three modes), while the heavier P atoms play an important role in the three acoustic
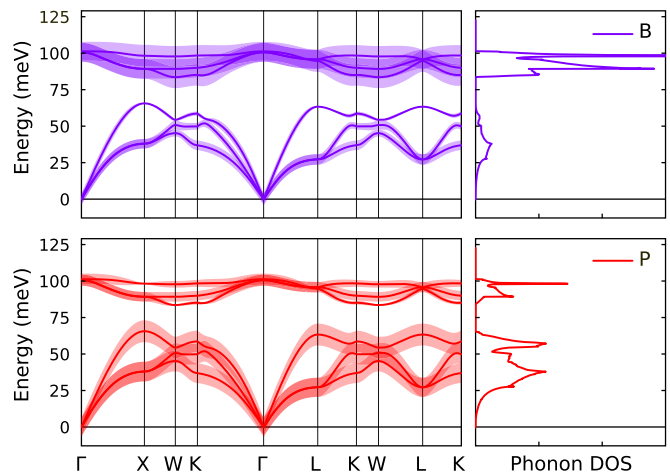

FIG. 2. Phonon dispersions, with fat bands representing atomic displacements associated with lattice vibrations. The width of the fat bands gives a qualitative understanding of which species are involved in the phonon modes. The projected DOS values of phonons on each type of atom are correspondingly shown next to the phonon dispersion. Here, the calculations are done using the semilocal PBE functional.

modes at low frequencies. The phonon dispersion computed using the HSE functional leads to a very similar dispersion with slightly higher phonon frequencies, particularly for the optical modes (see Fig. S1 of the Supplemental Material [66]).

The phonon-assisted optical absorption at 300 K, $\alpha(E)$, is shown in Fig. 3, which is calculated using the HSE functional for both electronic band structure and phonon dispersion. The indirect bandgap has a static lattice (with the assumption that nuclei do not vibrate around their equilibrium positions) value of 1.98 eV, while the direct optical gap is about 4.34 eV and therefore the energy range shown in Fig. 3 only corresponds to indirect absorption. As expected for indirect transitions, $\alpha(E)$
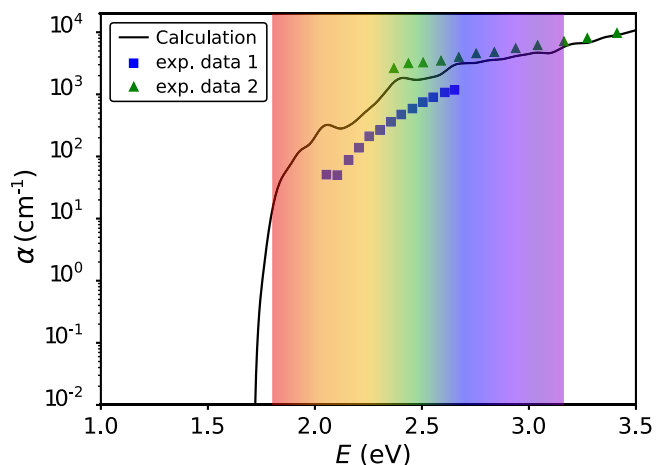

FIG. 3. Indirect absorption coefficient as a function of the photon energy calculated using the HSE functional at 300 K. Experimental data from Ref. [25] (exp. data 1) and Ref. [26] (exp. data 2) are also replotted for comparison. The color band indicates the visible spectrum.
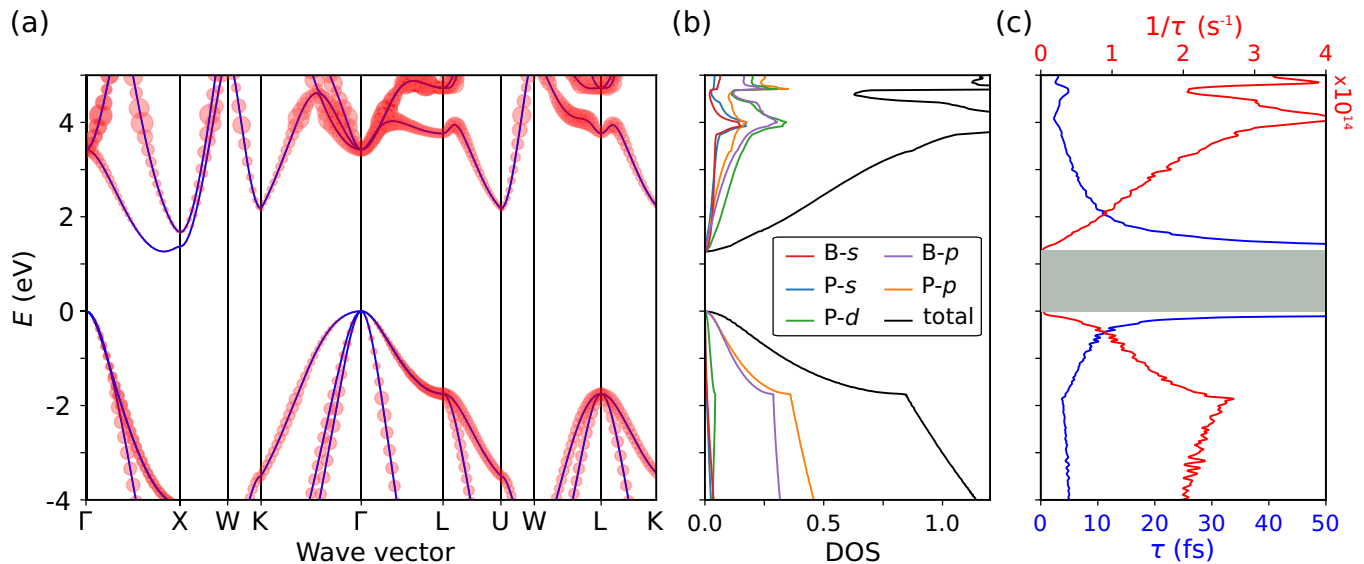
FIG. 4. (a) DFT electronic band structure at the PBE level, (b) projected DOS, and (c) relaxation time τ and scattering rate $1/\tau$. Each DFT electronic state is marked with a red circle representing its scattering rate by phonons at a temperature of 300 K (the intensity of scattering is proportional to the size of the circle). The projected DOS values are computed using DFT. The relaxation time τ (in fs) and its inverse, the scattering rate, $1/\tau$ (in units of s^{-1}), shown here as functions of the energy are calculated for undoped BP (the Fermi level is approximately set mid-gap).

is weak below the direct bandgap, with an average value of about 10^3 cm^{-1} in the visible range. The absorption onset at 300 K is red-shifted by about 0.25 eV in comparison with the indirect HSE static gap of 1.98 eV because the temperature dependence of the electronic band structure is also included in our calculations. The same observation was recently reported for one of the best *n*-type TCOs, BaSnO$_3$ [35]. We also include a comparison with experimental data from Refs. [25,26] in Fig. 3, which shows a reasonable agreement with our calculations. The remaining small differences might come from the approximation of the *ab initio* computational framework but might also very likely originate from sample quality issues in the experimental reports. It is noteworthy that this computational framework was utilized to compute indirect absorption for bulk silicon, yielding an excellent agreement with experiment [33]. We note that analogous calculations using the semilocal PBE functional lead to a qualitatively similar absorption profile, but with the significant red shift of about 1 eV associated with the standard bandgap underestimation of this semilocal functional.

Turning to electronic transport, Fig. 4(a) shows the DFT band structure and the scattering rates (inverse of $\tau_{n\mathbf{k}}$) at 300 K for different electronic states calculated using the PBE functional. The radius of the red circles accounts for the intensity of the scattering rate of the corresponding electronic state. We also present the projected and total DOS [Fig. 4(b)] and the corresponding relaxation time and scattering rate [Fig. 4(c)] as functions of the energy. In general, the scattering rates are proportional to the DOS, implying that the relaxation time becomes smaller in regions of high DOS. The Fermi level in doped BP can be located above or below the valence band maximum (VBM), depending on the number of holes and the density of states around this valley. For a hole concentration of 10^{18} cm^{-3}, the Fermi level is about 92 meV

above the VBM, while it is located about 273 meV below the VBM for the very high concentration of 10^{21} cm^{-3}. We calculated scattering rates for different doping concentrations (see Fig. S2 in the Supplemental Material [66]). From the band structure and the scattering rates, we can calculate the mobility at room temperature following Boltzmann transport theory. Figure 5 plots the hole mobility in BP as a function of the hole concentration at 300 K. The mobility decreases with the hole concentration because, as the Fermi level shifts below the VBM, the scattering rate increases [see Fig. 4(c) here and Fig. S2 in the Supplemental Material [66]). The hole mobility obtained at room temperature is about 900 cm^2/Vs
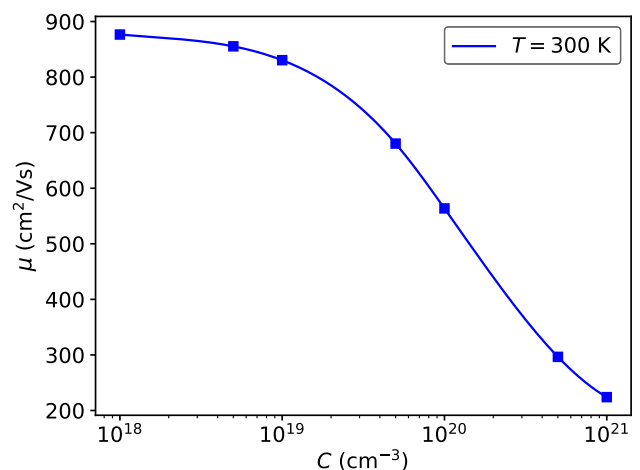

FIG. 5. Hole mobilities computed as a function of the hole concentration at 300 K. The curved line represents the interpolated data using the spline interpolation method.

TABLE I. Fabrication methods, hole-carrier concentrations C (in cm^{-3}), and mobilities μ (in cm^2/Vs) of cubic BP. These values are extracted from experimental measurements (with references cited) at room temperature. CVD, chemical vapor deposition.

Processing	C (cm^{-3})	μ (cm^2/Vs)	Remark
Solution (of Ni or Fe) growth	1.0×10^{18}	500 [73,74]	Contains 0.01% solvent
Epitaxial growth	8×10^{19}	285 [18]	Si substrate
Epitaxial growth	5×10^{19}	350 [18]	Si substrate
Heteroepitaxial growth	4.9×10^{19}	75.5 [19]	Si substrate
Heteroepitaxial growth	2.2×10^{19}	100.6 [19]	Si substrate
Chemical transport technique	1.67×10^{18}	1.77 [75]	Small amount of B$_6$P mixed
CVD + thermal neutron irradiation	1.1×10^{17}	100.3 [20,22]	Si substrate
Photothermal CVD	1.0×10^{17}	82 [76]	Si substrate

at a doping concentration of 10^{18} cm^{-3}. This very high mobility is the signature of a very low scattering rate. Indeed, other materials with similar/lower effective masses show mobilities at similar carrier concentrations and temperatures that are significantly lower. For comparison, we provide the data (including the calculated effective mass and mobility at a carrier concentration of 10^{18} cm^{-3} and a temperature of 300 K) for some materials in Table SI of the Supplemental Material [66]. Li$_3$Sb, which was also identified as a low-hole-effective-mass material, shows hole effective masses of 0.24 [17,67] which are lower than the values of 0.34 [16,67] in BP. However, the phonon-limited hole mobility of Li$_3$Sb is only around 70 cm^2/Vs [17]. A similar tendency is also observed in oxides, e.g., the well-known high-mobility *n*-type TCO, BaSnO$_3$. This compound has the extremely low electron effective mass of 0.13 [67,68] ($\sim$2.5 times smaller than the hole effective mass of BP) but, nonetheless, exhibits a calculated electron mobility (taking into account only longitudinal optical modes) of around 389 cm^2/Vs [69]. This is $\sim$2.3 times smaller than the hole mobility of BP.

The transport of holes in BP takes place around the Γ point and has contributions from three bands. In this region of the BZ, the scattering is very weak [see Fig. 4(a)], leading to high relaxation times around the VBM [see Fig. 4(c) here and Fig. S2 in the Supplemental Material [66]). We hypothesize that this weak scattering comes from a very weak scattering from polar modes. Indeed, the Born effective charges [70] computed for BP are very small [71]—about 0.56 for B and -0.56 for P—leading to weak long-range electron-phonon interactions [72]. Both Li$_3$Sb and BaSnO$_3$ are much more ionic. Li$_3$Sb shows Born effective charges of between 0.71 and 1.46 for Li and around -2.89 for Sb. BaSnO$_3$ Born effective charges are between 2.76 and 4.48 for the cations and between -3.51 and -1.86 for oxygen (see Table SI of the Supplemental Material [66]). Both BaSnO$_3$ and Li$_3$Sb should therefore show stronger scattering of electrons by polar phonons [72].

On a more general note, this indicates that nonoxide compounds, in addition to lower hole effective masses, can show lower phonon scattering rates than oxides. This arises directly from the possibility of nonoxides being less ionic and therefore offering weaker polar phonon scattering of the electrons.

The computed mobility is an upper bound to the experimental mobilities as it only takes into account intrinsic sources of scattering. We list in Table I a series of experimental

mobility measurements reported for boron phosphide. We note that some of the samples in these previous studies are not of a very high quality, and the measured mobility depends on the morphology of fabricated samples, such as whether they are single crystals, polycrystalline, amorphous, or thin films. Nevertheless, the experimental data confirm the potential for BP to deliver high mobilities.

Accordingly, our calculations show that boron phosphide offers a very high hole mobility ($\sim$900 cm^2/Vs) for a computed visible transmittance of 60% in a 100-nm film. Note that this relatively low transmittance is mainly due to the reflectivity of BP, which accounts for 39% of the loss of transparency. It is possible to use an antireflective coating to counter this problem [77,78]. If a hypothetically perfect antireflective coating is used so that the reflectivity of BP is suppressed, the transmittance increases up to 98% for a 100-nm film. This makes this material very attractive for transparent transistor applications. The possibility of *n*- and *p*-type doping of boron phosphide (as demonstrated both computationally and experimentally) strengthens even further its interest as a material for electronics applications in which ambipolar doping is a very useful property [79,80].

In many applications such as contacts for solar cells, it is not the mobility but the conductivity that is the transport quantity of interest. In those applications, a compromise between transparency and conductivity is often looked for and FOMs have been constructed to evaluate material performance as TCMs [60]. One of the most common FOMs has been proposed by Haacke [59]. It is obtained by multiplying the sheet conductivity by the transmittance to the power 10. FOMs are typically plotted versus the thickness to find the optimal thickness. Figure 6 shows Haacke's FOM versus thickness for one of the most traditional *p*-type transparent oxides, CuAlO$_2$ (in red), versus boron phosphide (in blue). The different lines indicate the different doping concentrations from 10^{20} to 10^{21} cm^{-3}. Here, the hole mobilities corresponding to various hole densities are interpolated from the computed data as shown in Fig. 5. Both materials show an optimal thickness around the micrometer length scale, but the achievable FOMs of BP are at least one order of magnitude larger. CuAlO$_2$ has a fundamental bandgap higher than 3 eV and therefore does not absorb light in the visible range. Despite BP absorbing in the visible, this occurs only through indirect transitions, and our analysis shows that the resulting low transparency is more than compensated by its higher conductivity in the overall FOM. Note that if reflectivity is suppressed in BP, its
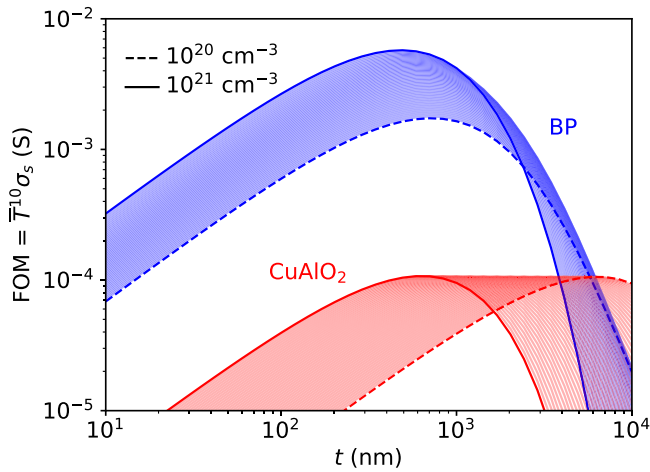
FIG. 6. Haacke FOM of BP (blue) and CuAlO$_2$ (red) as a function of the film thickness t. Dashed (solid) lines correspond to a hole concentration of 10^{20} (10^{21}) cm^{-3}.

FOM increases by two orders of magnitude. Overall, our study confirms the interest in boron phosphide as a *p*-type TCM and motivates further experimental work on this material and a reinvestigation of its growth and optoelectronic characterization [81].

IV. CONCLUSIONS

We have investigated the influence of phonons on the optical absorption and transport properties of BP using state-of-the-art *ab initio* methods. We observe very weak phonon-assisted optical absorption in the visible range. The hole mobility is estimated by solving the Boltzmann transport equation taking into account phonon scattering. Our results show that BP has an exceptionally high hole mobility ($\sim$900 cm^2/Vs at low doping and room temperature) for a transparent material. This very high hole mobility is due not

only to the low hole effective mass but also to the weak scattering of electrons by phonons. This weak scattering is attributed to the weak ionic nature of boron phosphide, leading to lower polar phonon scattering than in oxides. Our comparison of BP with established *p*-type TCMs such as CuAlO$_2$ indicates its much higher figure of merit and further confirms its potential as a *p*-type TCM. On a more general note, as nonoxides tend to be less ionic than oxides, they can lead to lower polar phonon scattering and higher mobilities. This is one additional reason to explore further nonoxides for TCM applications.

[1] H. Ohta and H. Hosono, Mater. Today **7**, 42 (2004).

[2] A. Facchetti and T. J. Marks (eds.), *Transparent Electronics: From Synthesis to Applications* (Wiley, New York, 2010).

[3] K. Ellmer, Nat. Photon. **6**, 809 (2012).

[4] P. Barquinha, R. Martins, L. Pereira, and E. Fortunato, *Transparent Oxide Electronics: From Materials to Devices* (Wiley, New York, 2012).

[5] E. Fortunato, P. Barquinha, and R. Martins, Adv. Mater. **24**, 2945 (2012).

[6] S. C. Dixon, D. O. Scanlon, C. J. Carmalt, and I. P. Parkin, J. Mater. Chem. C **4**, 6946 (2016).

[7] G. Hautier, A. Miglio, G. Ceder, G.-M. Rignanese, and X. Gonze, Nat. Commun. **4**, 2292 (2013).

[8] G. Brunin, F. Ricci, V.-A. Ha, G.-M. Rignanese, and G. Hautier, npj Comput. Mater. **5**, 63 (2019).

[9] H. Yanagi, J. Tate, S. Park, C.-H. Park, and D. Keszler, Appl. Phys. Lett. **82**, 2814 (2003).

[10] S. Park, D. A. Keszler, M. M. Valencia, R. L. Hoffman, J. P. Bender, and J. F. Wager, Appl. Phys. Lett. **80**, 4393 (2002).

[11] R. Woods-Robinson, J. K. Cooper, X. Xu, L. T. Schelhas, V. L. Pool, A. Faghaninia, C. S. Lo, M. F. Toney, I. D. Sharp, and J. W. Ager, Adv. Electron. Mater. **2**, 1500396 (2016).

[12] K. Ueda, S. Inoue, S. Hirose, H. Kawazoe, and H. Hosono, Appl. Phys. Lett. **77**, 2701 (2000).

[13] B. Williamson, G. Limburn, G. W. Watson, G. Hyett, and D. Scanlon (2019), 10.26434/chemrxiv.7078205.v2.

[14] J. B. Varley, V. Lordi, A. Miglio, and G. Hautier, Phys. Rev. B **90**, 045205 (2014).

[15] F. Yan, X. Zhang, Y. G. Yu, L. Yu, A. Nagaraja, T. O. Mason, and A. Zunger, Nat. Commun. **6**, 7308 (2015).

[16] J. B. Varley, A. Miglio, V.-A. Ha, M. J. van Setten, G.-M. Rignanese, and G. Hautier, Chem. Mater. **29**, 2568 (2017).

[17] V.-A. Ha, G. Yu, F. Ricci, D. Dahliah, M. J. van Setten, M. Giantomassi, G.-M. Rignanese, and G. Hautier, Phys. Rev. Mater. **3**, 034601 (2019).

[18] K. Shohno, M. Takigawa, and T. Nakada, J. Cryst. Growth **24-25**, 193 (1974).

[19] M. Takigawa, M. Hirayama, and K. Shohno, Jpn. J. Appl. Phys. **13**, 411 (1974).

[20] Y. Kumashiro, K. Kudo, K. Matsumoto, Y. Okada, and T. Koshiro, J. Less-Common Metals **143**, 71 (1988).

[21] Y. Kumashiro, M. Hirabayashi, and S. Takagi, MRS Proc. **162**, 585 (1989).

[22] Y. Kumashiro, J. Mater. Res. **5**, 2933 (1990).

[23] Y. Kumashiro, K. Nakamura, T. Enomoto, and M. Tanaka, J. Mater. Sci. Mater. Electron. **22**, 966 (2010).

[24] B. Stone and D. Hill, Phys. Rev. Lett. **4**, 282 (1960).

[25] M. Iwami, T. Tohda, and K. Kawabe, IEEJ Trans. Fund. Mater. **95**, 216 (1975).

[26] M. Odawara, T. Udagawa, and G. Shimaoka, Jpn. J. Appl. Phys. **44**, 681 (2005).

[27] C. Ambrosch-Draxl and J. O. Sofo, Comput. Phys. Commun. **175**, 1 (2006).

[28] F. Giustino, *Materials Modelling Using Density Functional Theory: Properties and Predictions* (Oxford University Press, New York, 2014), pp. 177–206.

[29] J. M. Ziman, *Principles of the Theory of Solids* (Cambridge University Press, Cambridge, UK, 1972), pp. 255–291.

[30] F. E. Williams, Phys. Rev. **82**, 281 (1951).

[31] M. Lax, J. Chem. Phys. **20**, 1752 (1952).

[32] E. P. Christopher and F. Giustino, J. Phys. Condens. Matt. **26**, 365503 (2014).

[33] M. Zacharias, C. E. Patrick, and F. Giustino, Phys. Rev. Lett. **115**, 177401 (2015).

[34] M. Zacharias and F. Giustino, Phys. Rev. B **94**, 075125 (2016).

[35] B. Monserrat, C. E. Dreyer, and K. M. Rabe, Phys. Rev. B **97**, 104310 (2018).

[36] Y. Kang, H. Peelaers, K. Krishnaswamy, and C. G. van de Walle, Appl. Phys. Lett. **112**, 062106 (2018).

[37] A. J. Morris and B. Monserrat, Phys. Rev. B **98**, 161203(R) (2018).

[38] I. Bravić and B. Monserrat, Phys. Rev. Mater. **3**, 065402 (2019).

[39] B. Monserrat, Phys. Rev. B **93**, 014302 (2016).

[40] B. Monserrat, J. Phys. Condens. Matter. **30**, 083001 (2018).

[41] G. Kresse and J. Hafner, Phys. Rev. B **47**, 558 (1993).

[42] G. Kresse and J. Hafner, Phys. Rev. B **49**, 14251 (1994).

[43] G. Kresse and J. Furthmüller, Comput. Mater. Sci. **6**, 15 (1996).

[44] G. Kresse and J. Furthmüller, Phys. Rev. B **54**, 11169 (1996).

[45] H. J. Monkhorst and J. D. Pack, Phys. Rev. B **13**, 5188 (1976).

[46] J. P. Perdew, K. Burke, and M. Ernzerhof, Phys. Rev. Lett. **77**, 3865 (1996).

[47] J. Paier, M. Marsman, K. Hummer, G. Kresse, I. C. Gerber, and J. G. Ángyán, J. Chem. Phys. **124**, 154709 (2006).

[48] J. H. Lloyd-Williams and B. Monserrat, Phys. Rev. B **92**, 184301 (2015).

[49] C. Kittel, *Introduction to Solid State Physics* (Wiley, New York, 2004), pp. 187–219.

[50] S. Baroni, P. Giannozzi, and A. Testa, Phys. Rev. Lett. **58**, 1861 (1987).

[51] X. Gonze, Phys. Rev. A **52**, 1086 (1995).

[52] F. Giustino, Rev. Mod. Phys. **89**, 015003 (2017).

[53] J. Noffsinger, F. Giustino, B. D. Malone, C.-H. Park, S. G. Louie, and M. L. Cohen, Comput. Phys. Commun. **181**, 2140 (2010).

[54] S. Poncé, E. R. Margine, C. Verdi, and F. Giustino, Comput. Phys. Commun. **209**, 116 (2016).

[55] P. Giannozzi, S. Baroni, N. Bonini, M. Calandra, R. Car, C. Cavazzoni, D. Ceresoli, G. L. Chiarotti, M. Cococcioni, I. Dabo, A. Dal Corso, S. de Gironcoli, S. Fabris, G. Fratesi, R. Gebauer, U. Gerstmann, C. Gougoussis, A. Kokalj, M. Lazzeri, L. Martin-Samos, N. Marzari, F. Mauri, R. Mazzarello, S. Paolini, A. Pasquarello, L. Paulatto, C. Sbraccia, S. Scandolo, G. Sclauzero, A. P. Seitsonen, A. Smogunov, P. Umari, and R. M. Wentzcovitch, J. Phys.: Condens. Matter **21**, 395502 (2009).

[56] P. Giannozzi, O. Andreussi, T. Brumme, O. Bunau, M. Buongiorno Nardelli, M. Calandra, R. Car, C. Cavazzoni, D. Ceresoli, M. Cococcioni, N. Colonna, I. Carnimeo, A. Dal Corso, S. de Gironcoli, P. Delugas, R. A. DiStasio, A. Ferretti, A. Floris, G. Fratesi, G. Fugallo, R. Gebauer, U. Gerstmann, F. Giustino, T. Gorni, J. Jia, M. Kawamura, H.-Y. Ko, A. Kokalj, E. Küçükbenli, M. Lazzeri, M. Marsili, N. Marzari, F. Mauri, N. L. Nguyen, H.-V. Nguyen, A. O. de-la Roza, L. Paulatto, S. Poncé, D. Rocca, R. Sabatini, B. Santra, M. Schlipf, A. P. Seitsonen, A. Smogunov, I. Timrov, T. Thonhauser, P. Umari, N. Vast, X. Wu, and S. Baroni, J. Phys.: Condens. Matter **29**, 465901 (2017).

[57] D. R. Hamann, M. Schlüter, and C. Chiang, Phys. Rev. Lett. **43**, 1494 (1979).

[58] G. K. H. Madsen and D. J. Singh, Comput. Phys. Commun. **175**, 67 (2006).

[59] G. Haacke, J. Appl. Phys. **47**, 4086 (1976).

[60] G. Brunin, G.-M. Rignanese, and G. Hautier, Phys. Rev. Mater. **3**, 064602 (2019).

[61] H. Kawazoe, M. Yasukawa, H. Hyodo, M. Kurita, H. Yanagi, and H. Hosono, Nature **389**, 939 (1997).

[62] H. Yanagi, S. Inoue, K. Ueda, H. Kawazoe, H. Hosono, and N. Hamada, J. Appl. Phys. **88**, 4159 (2000).

[63] R.-S. Yu, S.-C. Liang, C.-J. Lu, D.-C. Tasi, and F.-S. Shieu, Appl. Phys. Lett. **90**, 191117 (2007).

[64] J. Tate, H. L. Ju, J. C. Moon, A. Zakutayev, A. P. Richard, J. Russell, and D. H. McIntyre, Phys. Rev. B **80**, 165206 (2009).

[65] V.-A. Ha, D. Waroquiers, G.-M. Rignanese, and G. Hautier, Appl. Phys. Lett. **108**, 201902 (2016).

[66] See Supplemental Material at http://link.aps.org/supplemental/10.1103/PhysRevMaterials.4.065401 for phonon band structures, scattering rates and Born effective charge.

[67] F. Ricci, W. Chen, U. Aydemir, G. J. Snyder, G.-M. Rignanese, A. Jain, and G. Hautier, Sci. Data **4**, 170085 (2017).

[68] G. Hautier, A. Miglio, D. Waroquiers, G.-M. Rignanese, and X. Gonze, Chem. Mater. **26**, 5447 (2014).

[69] K. Krishnaswamy, B. Himmetoglu, Y. Kang, A. Janotti, and C. G. Van de Walle, Phys. Rev. B **95**, 205202 (2017).

[70] X. Gonze and C. Lee, Phys. Rev. B **55**, 10355 (1997).

[71] G. Petretto, S. Dwaraknath, H. P. Miranda, D. Winston, M. Giantomassi, M. J. van Setten, X. Gonze, K. A. Persson, G. Hautier, and G.-M. Rignanese, Sci. Data **5**, 180065 (2018).

[72] C. Verdi and F. Giustino, Phys. Rev. Lett. **115**, 176401 (2015).

[73] C. C. Wang, M. Cordova, and A. G. Fischer, RCA Rev. **25**, 159 (1964).

[74] T. L. Chu, J. M. Jackson, A. E. Hyslop, and S. C. Chu, J. Appl. Phys. **42**, 420 (1971).

[75] Y. Kumashiro, T. Yao, and S. Gonda, J. Cryst. Growth **70**, 515 (1984).

[76] Y. Kumashiro, K. Sato, S. Chiba, S. Yamada, D. Tanaka, K. Hyodo, T. Yokoyama, and K. Hirata, J. Solid State Chem. **154**, 39 (2000).

[77] I. Hamberg and C. G. Granqvist, J. Appl. Phys. **60**, 123 (1986).

[78] T. Fujibayashi, T. Matsui, and M. Kondo, Appl. Phys. Lett. **88**, 183508 (2006).

[79] J. B. Varley, A. Schleife, A. Janotti, and C. G. Van de Walle, Appl. Phys. Lett. **103**, 082118 (2013).

[80] N. F. Quackenbush, J. P. Allen, D. O. Scanlon, S. Sallis, J. A. Hewlett, A. S. Nandur, B. Chen, K. E. Smith, C. Weiland, D. A. Fischer, J. C. Woicik, B. E. White, G. W. Watson, and L. F. J. Piper, Chem. Mater. **25**, 3114 (2013).

[81] A. N. Fioretti and M. Morales-Masis, J. Photon. Energy **10**, 042002 (2020).